

An Electron beam-based Compton scattering x-ray source (ECoS) for OMEGA

Hans G. Rinderknecht,* G. Bruhaug, and G. Collins

Laboratory for Laser Energetics, University of Rochester, Rochester, NY 14620

(Dated: July 5, 2022, work in progress)

arXiv:2207.01549v1 [physics.plasm-ph] 4 Jul 2022

Abstract

The physics basis for an Electron Compton Scattering x-ray source (ECOS) is investigated for diffraction, Thomson scattering, and imaging experiments on the OMEGA laser. A source of monoenergetic ($\delta\epsilon/\epsilon < 5\%$) 10-50 keV x-rays can be produced by scattering of a short-pulse optical laser by a 23-53 MeV electron beam and collimating the scattered photons. The number and spectrum of scattered photons is calculated as a function of electron packet charge, electron and laser pulse duration, and laser intensity. A source with greater than 10^{10} photons in a 1 mm radius spot at the OMEGA target chamber center and 100 ps time resolution is plausible with available electron gun and laser technology. Design requirements for various experiments and opportunities for improved performance are discussed.

I. PHYSICS BASIS

Compton scattering is the canonical electrodynamic phenomenon of a charged particle scattering a high-energy photon. In the case of a relativistic electron beam with Lorentz factor $\gamma = (1 - \beta^2)^{-1/2} \equiv (1 + E/mc^2)$ interacting with a laser pulse, the apparent frequency of the photons in the reference frame of the electrons is increased by a factor $(1 + \beta)\gamma$. Assuming the electron's momentum is not significantly changed and the photon is forward scattered, returning to the laboratory frame applies this multiplier again, for a total increase in frequency and energy of approximately $4\gamma^2$. This quadratic scaling allows scattered optical photons ($E_i \sim 1$ eV) to reach the x-ray regime (> 1 keV) by scattering from an electron beam with $\gamma \gtrsim 16$ ($E \gtrsim 8$ MeV).

Accounting for relativistic electron orbits in a counterpropagating intense laser field, the scattered photon has a wavelength ω_f that depends on the initial laser wavelength ω_i and other terms as:[1]

$$\omega_f \approx \frac{2\gamma^2\omega_i(1 + \cos\phi)N_p}{1 + \gamma^2\theta^2 + \frac{a_0^2}{2} + 2\frac{\chi N}{a_0}} \quad (1)$$

Here, ϕ is the incident angle of the laser, $a_0 = eE/\omega_i mc \approx 0.86\sqrt{I_{18}\lambda_{\mu m}^2}$ is the normalized vector potential of the incident laser, $N_p \approx \max(1, a_0^3)$ represents the number of photons

* hrin@lle.rochester.edu

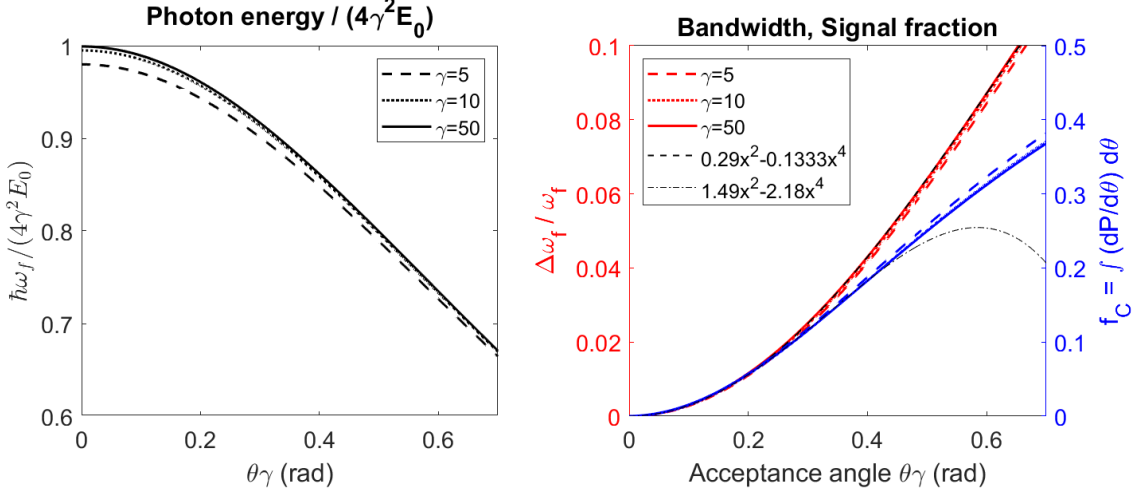


FIG. 1. (left) Normalized photon energy gain as a function of the product of detection angle θ and electron beam Lorentz factor γ ; (right) fractional bandwidth (red) and cumulative signal fraction (blue) for collimation acceptance angle $\theta\gamma$. Calculations assume head-on scattering ($\phi = 0$).

scattered per event, θ is the angle of the scattered photon relative to the electron beam direction, and $\chi \approx \gamma a_0 / a_{cr}$ represents the electric field strength in the electron rest frame normalized to the critical field $a_{cr} \approx 4.1 \times 10^5 \lambda_{\mu m}$. (For conditions discussed in this work, the last term will be negligible.)

Plots of the scattered photon energy in the limit of head-on scattering ($\phi = 0$) are shown in Figure 1a. Although the scattered photons are monoenergetic at any single detection angle, the bandwidth is a function of the collection solid angle that scales as $(\Delta\omega_f / \omega_f) \approx 0.29(\theta\gamma)^2 - 0.1333(\theta\gamma)^4$ in the range $\theta\gamma < 0.7$, as shown in Figure 1b. Integrating over the differential cross-section for scattering and transforming to the laboratory reference frame, the fraction of photons collected also scales with collection solid angle as $f_C \approx 1.49(\theta\gamma)^2 - 2.18(\theta\gamma)^4$ in the range $\theta\gamma < 0.4$. Details of this calculation are given in Appendix A 1. The efficiency of the source is limited by the required bandwidth: to achieve 1% (2%) intrinsic bandwidth requires collimation to $\theta\gamma \leq 0.19$ (0.27) rad, which in turn includes only 5% (10%) of the scattered photons. If the photon energy is tuned using the electron beam energy, the collimation will need to be adjusted to maintain optimal collection angle as a function of γ . Other sources of spectral broadening include:[2]

$$\frac{\Delta\omega_f}{\omega_f} \approx \sqrt{\left(\frac{\Delta\omega_i}{\omega_i}\right)^2 + \left(\frac{2\Delta\gamma}{\gamma}\right)^2 + \left(\frac{0.88a_{0,\text{eff}}^2}{2 + a_{0,\text{eff}}^2}\right)^2 + \left(\frac{1.05(\gamma\sigma_{\theta,\text{eff}})^2}{1 + (\gamma\sigma_{\theta,\text{eff}})^2}\right)^2} \quad (2)$$

Here, $a_{0,\text{eff}}$ is the effective normalized vector potential, weighted by the local number of photons in the laser pulse, and $\sigma_{\theta,\text{eff}}$ is the electron beam divergence weighted over the laser pulse. The x-ray bandwidth scaling with laser and electron bandwidth follows directly from the numerator of Eq. 1. The quadratic scaling with laser intensity a_0 arises from a reduction in the instantaneous energy of the electron beam within the laser packet due to the ponderomotive force. (This form assumes a Gaussian laser packet.) To maintain a scattered photon bandwidth of 1%, Eq. 2 suggests the intensity must be limited to $a_{0,\text{eff}} < 0.15$. With control of the laser temporal and spectral properties this effect may be limited, allowing monoenergetic scattering with more intense beams.

The number of photons scattered per laser cycle N_x is given by:[1, 3]

$$\frac{N_x}{\nu_i^{-1}} \sim \begin{cases} 1.53 \times 10^{-2} a_0^2, & a_0 < 1 \\ 3.31 \times 10^{-2} a_0, & a_0 \gg 1 \end{cases} \quad (3)$$

The number of photons scattered by a relativistic electron charge packet interacting with a laser pulse can be estimated as the product of Eq. 3 with the number of electrons in the packet and number of laser cycles. The number of laser cycles observed by the electrons (N_τ) may depend on the temporal and spatial properties of the focused laser pulse. Assuming a diffraction-limited spot, if the Rayleigh length is long compared to the pulse duration τ_L (that is, $z_R = 4f_\#^2\lambda/\pi \gg \tau_L c$), then the temporal profile will limit the interaction, the number of laser cycles will be $\tau_L \omega_i / 2\pi$. Otherwise, the geometry of the interaction will limit the number of laser cycles to $2z_R/\lambda = 8f_\#^2/\pi$ or $0.75f_\#/\phi$, whichever is smaller. (The derivation of the geometric terms is described in Sec A 2.) In these cases, assuming the laser is in the regime $a_0 < 1$, the number of scattering events is approximately:

$$N_{x,\text{tot}} = f_C N_e \left(\frac{N_x}{\nu_i^{-1}}\right) N_\tau \approx 10^9 \left(\frac{\theta\gamma}{0.27}\right)^2 \left(\frac{Q}{1 \text{ nC}}\right) a_0^2 \begin{cases} 2.31 \left(\frac{\hbar\omega_i}{1 \text{ eV}}\right) \left(\frac{\tau_L}{1 \text{ ps}}\right), & \tau_{LC} \ll z_R \\ 2.43 \min\left[1, \frac{0.294}{f_\#\phi}\right] \left(\frac{f_\#}{10}\right)^2, & \tau_{LC} \gg z_R \end{cases} \quad (4)$$

Typically, the latter condition will hold, as $z_R/c = 0.26 \text{ ps}$ for $f_\# = 10$. The number of

scattered photons is maximized with high charge, high intensity, and longer laser pulses or longer focal lengths.

The use of a flying focus laser may improve the performance by decoupling the length of the scattering volume (L) from the radius of the focal spot (σ_L). [4] This makes more efficient use of laser energy. With a flying focus pulse, the number of cycles is simply L/λ and the number of scattering events is:

$$N_{x,FF} = 7.7 \times 10^9 \left(\frac{\theta\gamma}{0.27} \right)^2 \left(\frac{Q_e}{1 \text{ nC}} \right) \left(\frac{L}{1 \text{ mm}} \right) \left(\frac{\hbar\omega_i}{1 \text{ eV}} \right) \begin{cases} a_0^2, & a_0 < 1 \\ 2.2a_0, & a_0 \gg 1 \end{cases} \quad (5)$$

Moreover, the bandwidth dependence on intensity (a_0^2) is produced by the gradient in intensity and assumes a Gaussian pulse. A flying focus can produce a roughly flat intensity equal to the peak intensity that travels with the electron packet over a long distance. This should reduce the a_0 -dependent bandwidth term by the ratio of the rise and fall region divided by the length: $2a_0/\max(\nabla a_0)L$. However, the size of the electron packet that fits inside the co-moving intense region will be limited by the Rayleigh length of the laser. This relationship is discussed in Sec. II C.

For Equations 4-5, the useful fraction of scattered photons is limited by bandwidth considerations to roughly $f_C \lesssim 0.1$ (see Fig. 1b). The temporal resolution of the source will be set by the transit time of the electron packet through the laser pulse. For head-on collisions ($\theta \sim 0$), this duration is set by the larger of the two. The charge available in a photoinjector electron gun is limited by space charge and scales with the duration of the packet ($\tau_e = w/c$, for packet width w). An optimal design would then have laser and electron pulse durations equal at approximately the desired temporal resolution, to maximize both the bunch charge and the number of laser cycles.

In the following sections we will consider available electron gun and laser technology to assess the potential for an implementation at OMEGA.

II. SOURCE PROPERTIES

A. Electron Photoinjectors

Electron photoinjectors are a commercial technology enabling ultrafast MeV-scale electron bunches. [5] In these systems, a UV laser (typically with μJ energy) irradiates a photo-

cathode to produce electrons, which are then accelerated using a small radiofrequency (RF) waveguide to several MeV. The photoinjector and first acceleration stage (5 MeV) of a commercial system is typically less than 1 meter in length. Further accelerating sections can be introduced to reach higher energies, with typical acceleration gradients above 100 MV/m. Additional magnetic optics may be used to improve and control beam quality, such as pulse compression or focusing. Pulse temporal compression can be achieved using chicanes (a sequence of dipole magnets) or RF cavities.

1. *Packet charge and width*

Several examples exist in the literature of sources producing 10's nC of electrons in 10's ps bunches. The A \emptyset Photoinjector at Fermilab produces 16 MeV, 10–14 nC electron bunches with uncompressed length < 40 ps.[6] A subsequent compression by 9-cell cavity RF stage can reduce the pulse length to under 10 ps. The ELSA facility at CEA includes a photoinjector source that can produce 14 nC bunches in 90 ps lengths using a 1.2 μJ , 60 ps laser pulse.[7] These bunches are accelerated to 16 MeV in the first stage of the linac (~ 7 meters). From the scaling in Eq. 4, bunch charges on the 10 nC, 100 ps level are relevant to producing Compton x-ray sources with on the order of 10^{10} photons.

A multi-bunch photo-cathode RF gun system has been demonstrated.[8] A 357 MHz (2.8 ns separation) pulse train of 266 nm UV (4ω) laser light with 5 μJ per pulse was used to irradiate the photocathode. The accelerating RF with a driving frequency of 2856 MHz, or $8\times$ the laser pulse frequency, was driven with up to 17 MW input power from a pulsed klystron. Total charge up to 3.5 nC per packet were observed, accelerated to 5 MeV with 1% momentum spread between packets. This work suggests that such a system may provide the basis for a multi-pulse x-ray source with ns-scale pulse separation. As the resulting x-ray pulses would be co-linear, a single line-of-sight (SLOS) time-resolving camera would be required to differentiate between signal pulses.[9]

2. *Emittance*

Divergence of the electron beam σ_θ produces broadening in the spectrum proportionally to $\gamma\sigma_\theta$ (Eq. 2). Here, the divergence is defined as the RMS average of the incident electron

angle relative to the beam axis. The quality of an electron beam is usually characterized by the emittance $\varepsilon = \beta\gamma\sqrt{\langle x^2 \rangle \langle x'^2 \rangle - \langle xx' \rangle^2} \approx \beta\gamma\sigma_x\sigma_\theta$ in terms of the RMS beam size σ_x and divergence σ_θ . The measured emittance of the sources described above are 20π mm mrad (Fermilab A0) and <4 mm mrad (CEA ELSA), respectively.[6, 7] To limit spectral broadening due to beam emittance below 1% (2%) requires $\gamma\sigma_{\theta,\text{eff}} \lesssim 0.1$ (0.14) rad, respectively. With an ELSA-quality beam, this level of divergence could be attained with a beam spot size $\sigma_x = \varepsilon/\beta\gamma\sigma_\theta \approx 40 \mu\text{m}$ ($29 \mu\text{m}$) at focus. The smaller value between this and the laser focal spot size will define the x-ray source size, which in turn defines the resolution for imaging applications.

Lower emittance has been achieved in some systems with reduced bunch charges. The ELSA photoinjector achieved values as low as 1 mm mrad at $Q = 1$ nC, which was close to the thermal emittance of the cathode.[7] The BriXS Ultra High Flux inverse Compton source reports packets of 100-200 pC in 1.3-4.0 ps bunches with nominal normalized emittance in the range 0.6-1.5 mm mrad.[10] A brief literature search suggested that comparably low-emittance bunches are limited to roughly the range 50–200 pC per ps pulse duration.[11] In interactions with a flying focus, where shorter pulses are required, we will assume values of $\varepsilon = 1$ mm mrad and $Q = (100 \text{ pC/ps})\tau$ may be reasonably expected.

3. Bandwidth

Radiofrequency acceleration is self-correcting for electron energy dispersion and in general achieves very small bandwidth variations. For example, the CEA ELSA accelerator described above produces 0.1% RMS energy dispersion.[7] Limiting the electron energy spread to less than 1% should not be challenging and the bandwidth of the resulting x-ray source should not be dominated by the $(\Delta\gamma/\gamma)$ term.

B. Laser Sources

In the case of laser pulses with Gaussian temporal history, monoenergetic scattered x-rays ($\Delta\omega_f/\omega_f \leq 1\%$) require a limit on the normalized vector potential of $a_0 < 0.15$, which limits the intensity as $I < 3 \times 10^{16} \text{ W/cm}^2 (\lambda_{\mu\text{m}})^{-2}$. This level of intensity in a 100 ps pulse duration with a focal spot of with $40 \mu\text{m}$ radius would require 150 Joules of 1053 nm

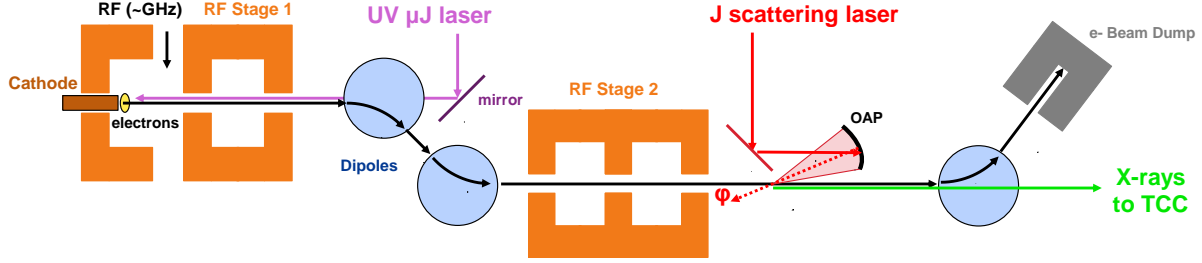


FIG. 2. Schematic of an electron-beam Compton scattering x-ray source for OMEGA.

laser light, with peak power of 1.5 TW. Use of a higher frequency laser at the same a_0 and τ_L would linearly increase the number of scattered photons (Eq. 4) and also the scattered photon frequency (Eq. 1). This would, however, require an increase in the laser intensity proportional to ω_i^2 .

A flying focus pulse would make more efficient use of the laser energy. To achieve $3e16 \text{ W/cm}^2$ in a focal spot with $40 \mu\text{m}$ radius and length of 1 mm would require roughly 5 Joules. However, the intense region would be a smaller region co-moving with the electron packet. Because of this, an electron packet with 10 ps duration (3 mm in length) would mostly not overlap with the light, limiting the electron charge involved in the interaction. This may still have an advantage, if the lower-charge electron beam may feature improved emittance and interact on average with higher intensity, and will be considered in the next section.

C. Beam-laser interaction

A schematic diagram of an electron beam-based Compton x-ray source is shown in Figure 2. The primary engineering challenge of the source is co-timing and co-aligning the electron beam and the scattering laser pulse. At a minimum, the two beams must be co-timed better than the longer of the two pulse durations, and co-aligned better than the larger of the packet waist and the focal spot size. Assuming the system is designed to achieve 100 ps temporal resolution, a timing jitter on the order of 10 ps will be required, equivalent to 3 mm of laser path. To robustly achieve this level of co-timing, a single laser front-end should seed both the μJ UV laser that irradiates the photocathode and the scattering laser.

The creation of high-charge beams is more likely to be a limiting factor than laser in-

tensity. The most robust design will therefore feature a laser pulse that is both longer and spatially larger than the electron packet, such that the spatial resolution of the system is set by the electron packet size and the temporal resolution by the transit time. Note that the geometric terms in Eq. 4 strongly encourage an on-axis scattering geometry. If the laser is coaxial with the electron beam ($\phi = 0$), the geometric term for spatially-limited scattering increases as $f_{\#}^2$, encouraging long scattering distances. But if the offset from on-axis scattering exceeds $\phi > 2/\pi f_{\#}$ ($= 3.6^\circ$ for $f_{\#} = 10$), the intersection volume grows only linearly with $f_{\#}$. In the case of flying focus (Eq. 5) the standard optics require on-axis scattering for the intense region to co-move with the electron packet. For these reasons, an on-axis scattering geometry is highly beneficial for both cases.

III. IMPLEMENTATION AT OMEGA

The simplest design for an ECoS x-ray source at OMEGA would locate the electron acceleration stages and laser interaction chamber next to the OMEGA target chamber with a fixed port location. In this design, the electron beam is dumped outside of the OMEGA target chamber, and only a collimated x-ray beam is injected into the chamber. A benefit of this design is the ability to dump the electron beam and scattering laser far from the sensitive diagnostic instruments around the target chamber. However, this design limits the x-ray flux on the laser-driven target, as the scattering event would occur several meters from TCC. Taking the optimal collimation for $f_C = 10\%$ collection of scattered photons as $\theta\gamma \lesssim 0.27$ radians, photons of 10 (50) keV (that is, $\gamma = 46$ (103) if the scattering laser wavelength is 1 μm) require collimating angles of 5.9 (2.6) mrad, respectively. If the interaction occurs 3 m from target chamber center, which is the distance of the rear of a TIM, the collimated beam would then project to a radius of 18 (8) mm at TCC: almost an order of magnitude larger than a typical target. Increased collimation would reduce bandwidth at the cost of signal: a 1 mm beam at TCC would imply collimation of 0.33 mrad and collect less than 0.1% of the scattered signal.

This problem could be mitigated by the use of long wavelength lasers, compensated by higher electron beam energy. A CO_2 laser ($\lambda = 10 \mu\text{m}$) would produce 10-50 keV photons by scattering from an electron beam with $\gamma = 142$ -318. Optimal collimation would capture 1.9-0.85 mrad, projecting to 5.7-2.5 mm at TCC, respectively. While this is somewhat improved



FIG. 3. Cartoon of laser-electron interaction region for case with the final laser optic on the opposite side of TCC from the electron beam. This image assumes $\phi = 2^\circ$ and electron deflection angle 3° ($B \sim 1$ T).

over the prior case, the signal is still larger than most targets. Moreover, this comes at the cost of a considerably larger and higher-energy electron gun: up to 162 MeV.

Assuming a $1 \mu\text{m}$ laser is used, matching the beam to the target size requires the Compton scattering to occur closer to TCC. A beam radius less than 1 mm for photons above 10 keV would require the scattering to occur roughly 15 cm from TCC. In this system, the electron beamline would inject into the OMEGA target chamber at a fixed port location. Beam steering and shaping magnets would point the beam to TCC and control its focus. In this arrangement, the scattering laser cannot be injected directly opposite the electron beam, as the target is in the way. Two options are available: the final optics of the scattering laser can be on the opposite side of the target chamber with a non-zero incidence angle ϕ to avoid TCC, or the final optics may be positioned co-linear with the electron beam on the near side of TCC. These cases are considered below.

If the laser final optic is on the opposite side of the target chamber from the electron beam, clearing the target at TCC would require a scattering angle of $\phi \sim \tan^{-1}(5\text{mm}/150\text{mm}) \approx 0.033$ rad (2°) and a beam focus $f_{\#} > 1/\tan(2\phi) \sim 15$. Following Eq. 4, the scattered photon number would increase quadratically with focal length up to $f_{\#} = 20$, and linearly above that. This arrangement has the disadvantage that plasmas near TCC may perturb the beam transport, and that the quadratic increase in scattering volume with longer focal lengths cannot be leveraged. This scenario is depicted in Figure 3.

If the final optic is on the electron beam axis prior to TCC, its position must take into account the electron beam dump magnet and the x-ray collimator. To use the system on cryogenic target implosions, all hardware must be at least 10 cm from TCC on an equatorial line of sight (the distance increases for non-equatorial views). The maximum

distance between the final optic and the scattering location is then $D = 5$ cm. Intensity on this final optic will scale as the intensity at best focus times a geometric ratio $R = f_{\#}^4 \lambda^2 / D^2$. For $D = 5$ cm, $\lambda = 1$ μm , and $f_{\#} = 10$, this ratio is 4×10^{-6} and an $a_0 = 0.15$ ($I = 2.8e16$ W/cm²) beam will produce an intensity of 10^{11} W/cm² on the mirror. This intensity is approaching the threshold for optics damage, so use of a plasma mirror for this final stage may be beneficial. A plasma mirror is capable of reflecting light at above TW/cm² intensity, which would enable placing the final mirror closer to the scattering point and using longer focal lengths. A shaped convex plasma mirror could potentially be used to upconvert the $f_{\#}$ of the final beam, achieving much longer interaction volumes than are otherwise possible. A cartoon of this scenario is depicted in Figure 4. Because flying-focus laser intensity is generally elongated along the axis of the final optic, this geometry would be needed for a flying-focus based source.

Assuming an ELSA-like electron source, the performance of this design is detailed in Table I. To match the electron bunch radius of 40 μm and duration of 90 ps, a laser energy of 133 J and focal length of $f_{\#} = 61$ were required. The energy and focus are comparable to the BELLA laser (40 J, $f/65$) although that system delivers much shorter pulses (30 fs). The energy and pulse length are less than an OMEGA-EP short-pulse beam (1-2 kJ, 100 ps) but with a much longer focal length. Note that this design is in the spatial limit of Eq. 4 because $2z_R < \tau_{LC} \approx$. The on-axis design, which requires a final optic on the same side of TCC as the electron beam, produces 2.9×10^{10} scattered photons. An opposite-TCC design with an impact angle $\phi = 2^\circ$ reduces the number of interacting laser cycles by $\sim 0.14\times$ compared to on-axis scattering, due to geometric effects.

Improving the electron beam emittance would reduce the bunch radius as ϵ . This would

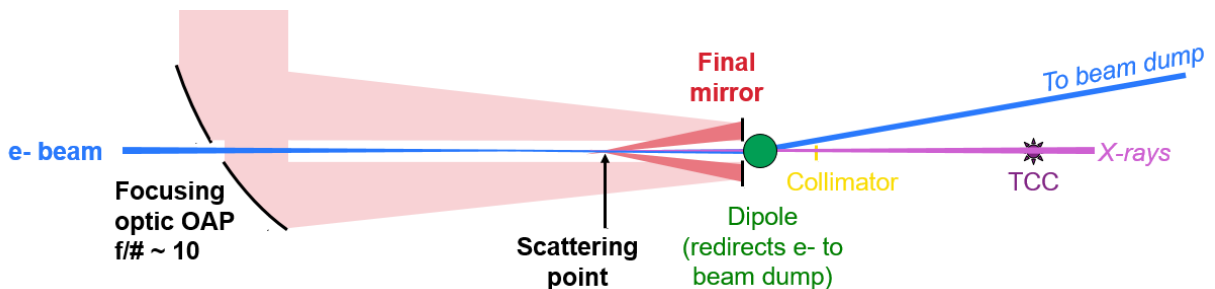


FIG. 4. Cartoon (not to scale) of laser-electron interaction region for case with the final laser optic on the same side of TCC as the electron beam.

in turn reduce the required focal length as ε and the required laser energy as ε^2 . However this would also reduce the Rayleigh length by $f_{\#}^2$, resulting in less scattering overall. In general, the number of scattered photons benefits from larger $f_{\#}$ (for longer interaction distances), which produces larger spots and requires higher laser energy as $E_L \propto f_{\#}^2$. Overfilling the electron packet with the laser may be beneficial as this maintains the number of scattered photons and the source resolution ($\sigma_{x,e}$) while reducing the difficulty of alignment. Alternatively, the laser could be focused to a smaller spot than the electron packet, increasing the resolution and relaxing the bandwidth constraint due to $\gamma\sigma_{\theta,\text{eff}}$. However this would reduce the number of electrons available for scattering ($\propto (w_0/\sigma_{x,e})^2$) and the scattering path length.

A calculation for a flying focus design is also shown in Table I. This design produces comparable scattering performance with a substantially reduced electron bunch charge (100 pC) due to the high intensities ($a_0 = 1$) and long interaction lengths (20 mm). The spatial resolution is also improved to $\sim 10 \mu\text{m}$, and the focal length is reduced to $f_{\#} = 15$. However, approximately twice as much laser energy (269 J) is required to create the desired laser focus. This design requires on-axis focusing. Due to the higher intensities involved, a plasma mirror would likely be needed for the final optic.

A magnetic deflection system between the scattering region and TCC would steer the electrons away from TCC to a beam dump on the opposite side of the chamber. A collimator would also be needed to block non-monochromatic photons produced at larger scattering angles. Challenges of this scenario include co-timing of the electron beam and scattering laser, and alignment of the beam, laser, and collimator.

Given typical gradients and the relatively modest energies of interest (up to 50 MeV), a custom accelerator might be designed to fit within the space limitations of a TIM. However, engineering challenges, such as transporting short-pulse laser light to the photocathode and RF waves into the acceleration cavity, might prove prohibitive.

A. Beam dump requirements

To prevent the electron beam impacting the experiment at TCC, the electrons must be deflected to a beam dump. A magnetic dipole field produced by a MIFED-like capacitor discharge system may be fielded between the scattering region and TCC. The deflection

Quantity	symbol	Gaussian laser		Flying focus	
X-ray energy	$\hbar\omega_f$	20 keV		10 keV	50 keV
Electron beam energy	$E_e(\gamma)$	32.8 MeV (65.2)		23 MeV (46)	52 MeV (103)
Collimation angle	θ_{col}	4.2 mrad		6.0 mrad	2.7 mrad
Bunch charge	Q_e	14 nC		0.1 nC	
Bunch width	τ_e	90 ps		1.0 ps	
Emittance	ε	4 mm mrad		1 mm mrad	
Bunch radius	$\sigma_{x,e}$	41 μm		10 μm	
Electron bandwidth	$\Delta\gamma/\gamma$	0.001		0.001	
Laser wavelength	λ_0	1053 nm		1053 nm	
Laser bandwidth	$\Delta\omega_i/\omega_i$	0.001		0.01	
Laser focus	$f/\#$	61		15	
Focal spot radius	w_0	41 μm		10 μm	
Rayleigh length	z_R	5.0 mm		310 μm	
Laser duration	τ_L	90 ps		67 ps (chirped)	
Peak Intensity	$a_0(I)$	0.15 (2.8×10^{16} W/cm ²)		1.0 (1.2×10^{18} W/cm ²)	
Laser energy	E_L	133 J		269 J	
Impact angle	ϕ	0 mrad (0°)	35 mrad (2°)	0 mrad (0°)	
Interaction length	L	9.9 mm	1.4 mm	20 mm	
# photons	$N_{x,tot}$	2.9×10^{10}	4.0×10^9	1.9×10^{10}	
Bandwidth	$\Delta\omega_f/\omega_f$	2.5%		2.5%	

TABLE I. Expected performance of a source for x-ray Compton scattering on OMEGA.

must occur prior to x-ray collimation, because if the electrons were to strike the high-Z collimator foil this would produce a large, broadband bremsstrahlung source that would likely overwhelm the Compton scattering signal. The angle of deflection ζ for relativistic electrons traversing a magnetic field is given by the scaling $\sin \zeta \approx (BL/3.33 \text{ T cm})(E_e/10 \text{ MeV})^{-1}$. A deflection of 3° would avoid striking the experiment from a distance of 10 cm, requiring a magnetic field integral of at least 0.9 T cm. This is readily achievable using a MIFEDs-like system. For electron beams at lower energy, the coil field can be detuned to ensure the electron beam reaches a beam dump located on nearly the opposite side of the target chamber

wall from the electron source.

B. Collimation requirements

Collimation of the x-ray source is needed to achieve narrow bandwidth, as shown in Figure 1b. The e-folding attenuation depth for 50 keV x-rays in Tungsten (Tantalum) is 87 (105) microns, respectively. Attenuation to $< 1\%$ of the signal can therefore be achieved by a 0.5 mm thick foil fielded between the source and TCC at a distance d from the source. The radius of the collimating aperture is $d \tan \theta_{max} \approx 0.27d/\gamma$ for 2% bandwidth. For the highest-energy x-rays, $\gamma \approx 100$ and the required aperture radius scales as $27 \mu m \times (d/cm)$. Coalignment of the electron source, aperture, and TCC must be achieved to on the order of the collimator radius. This requirement becomes easier for larger d . Assuming an electron beam repetition rate above 1 Hz, alignment of the electron beam and collimator may be achieved by irradiating a scintillator or phosphorescent source at TCC with electrons transiting the collimator.

IV. APPLICATIONS

A. X-ray Diffraction

The present state-of-the-art x-ray diffraction experiments on OMEGA use laser-driven metal foils as He- α x-ray backlighters.[12–14] These sources are capable of producing monoenergetic x-rays up to roughly 10 keV. In order to maximize x-ray production, up to 2 ns laser pulses are used to drive the backlighters. This limits the applicability of the diagnostic to HED materials compressed by comparably long laser pulses, and prevents their use on spherically imploded targets that can reach higher pressure states. Under these conditions, Fe backlighters can probe the samples with 10^{12} photons per experiment,[13] however efficiency decreases with increasing atomic number so higher energies cannot be effectively used. Optimized Radiation from the backlighter and x-ray sources also produce substantial background on the detector at and above the energies of interest that must be subtracted to extract the signal. High intensities needed to produce efficient He- α line radiation also produce hot electrons by laser-plasma interaction physics (LPI) that result in a broad, hard x-ray background.[15]

An ECoS backlighter would improve x-ray diffraction studies with higher energy x-rays (20 – 50 keV) and improved time resolution (<100 ps). Use of the Compton scattering source would eliminate the hot-electron background associated with the x-ray source foil. Sampling with x-rays above 20 keV would allow an increase in the detector shielding that would reduce x-ray background from the driven sample ($T \sim \text{few keV}$). Together, these improvements would reduce the background in the data by more than 2 orders of magnitude. This benefit would compensate for the reduction in scattering signal; however, at least 10^{10} photons in the source would likely be required.

B. X-ray Imaging

The requirements of X-ray imaging are quite different from diffraction and Thomson scattering. Beam dispersion is beneficial, as this leads to magnification of the image and simplifies diagnosis. For point-projection imaging, the resolution would be set by the size of the source, which is the smaller of the electron packet width and the scattering laser focal width. However, given the increase in bandwidth with reduced electron packet radius, for imaging it may be best to neglect the monoenergetic scattering in favor of point projection. If the electron beam may be focused to a small point $\sigma_x \sim 1 \mu\text{m}$, it will have a divergence $\sigma_\theta = \varepsilon/\beta\gamma\sigma_x \approx 50 \text{ mrad}$ for an ELSA-like beam. This increased divergence increases the magnification of the image. Since Compton scattering would in any event produce a broadband spectrum in this case ($\gamma\sigma_\theta \sim 1$), one option would be to directly irradiate a high-Z foil with the electron beam. This will produce a broad-band intense bremsstrahlung backlighter, with x-ray energy of 100's of keV.

Appendix A: Derivations

1. Photon Energy and Scattering Probability in the Laboratory Frame

The differential cross-section for scattering in the rest frame of the electron is given by the Klein-Nishina formula:

$$\frac{d\sigma_{KN}}{d\Omega} = \frac{r_0^2}{2} \left(\frac{\omega_f}{\omega_i} \right)^2 \left(\frac{\omega_f}{\omega_i} + \frac{\omega_i}{\omega_f} - \sin^2 \theta_s \right) \quad (\text{A1})$$

where r_0 is the classical electron radius and θ_s is the scattering angle of the photon. Notably, the ratio of final to initial frequency is determined entirely by scattering angle and incident photon energy:

$$\frac{\omega_f}{\omega_i} = \frac{1}{1 + \frac{\hbar\omega_i}{m_e c^2} (1 - \cos \theta_s)} \quad (\text{A2})$$

The total cross section is roughly 53 mb for low-energy scattering, and drops as $\hbar\omega_i$ approaches and exceeds the electron rest mass.

The relativistic calculation of the photon energy and flux as a function of laboratory angle is most straightforward using the four-vector notation, in which the energy and momentum of the photon \vec{k} and the Lorentz transformation matrix L are:

$$\vec{k} = \frac{\epsilon}{c} \begin{bmatrix} 1 \\ \sin \theta_L \cos \phi_L \\ \sin \theta_L \sin \phi_L \\ -\cos \theta_L \end{bmatrix} \quad (\text{A3})$$

$$L(\vec{\beta}) = \begin{bmatrix} \gamma & -\gamma\beta_x & \gamma\beta_y & \gamma\beta_z \\ -\gamma\beta_x & 1 + (\gamma - 1)\frac{\beta_x^2}{\beta^2} & (\gamma - 1)\frac{\beta_x\beta_y}{\beta^2} & (\gamma - 1)\frac{\beta_x\beta_z}{\beta^2} \\ -\gamma\beta_y & (\gamma - 1)\frac{\beta_y\beta_x}{\beta^2} & 1 + (\gamma - 1)\frac{\beta_y^2}{\beta^2} & (\gamma - 1)\frac{\beta_y\beta_z}{\beta^2} \\ -\gamma\beta_z & (\gamma - 1)\frac{\beta_z\beta_x}{\beta^2} & (\gamma - 1)\frac{\beta_z\beta_y}{\beta^2} & 1 + (\gamma - 1)\frac{\beta_z^2}{\beta^2} \end{bmatrix} \quad (\text{A4})$$

for photon energy $\epsilon = \hbar\omega$ and incident laser direction (θ_L, ϕ_L) .

To calculate the properties of the scattered photons, the following procedure is performed. Initial laser photons \vec{k}_i are boosted into the electron rest frame by applying the Lorentz transformation: $\vec{k}'_i = L(\vec{\beta}_0)\vec{k}_i$. (Primes indicate boosted quantities.) The scattering is calculated using Equations A1 and A2, resulting in a new energy and trajectory for the photon, \vec{k}'_f . The scattered photons are boosted back into the laboratory frame: $\vec{k}_f = L(-\vec{\beta}_0)\vec{k}'_f$.

Without loss of generality we choose $\phi_L = \pi/2$ and initial electron velocity $\vec{\beta}_0 = \beta_z \hat{z}$. This results in a boosted photon a four-momentum:

$$\vec{k}'_i = \frac{\epsilon_i}{c} \begin{bmatrix} \gamma(1 + \beta \cos \theta_L) \\ 0 \\ \sin \theta_L \\ -\gamma(\beta + \cos \theta_L) \end{bmatrix} \equiv \frac{\epsilon'_i}{c} \begin{bmatrix} 1 \\ 0 \\ \sin \theta'_L \\ -\cos \theta'_L \end{bmatrix} \quad (\text{A5})$$

where we have defined the boosted energy $\epsilon'_i = \epsilon_i \gamma (1 + \beta \cos \theta_L)$ and the boosted incident laser angle $\sin \theta'_L = \sin \theta_L / \gamma (1 + \beta \cos \theta_L)$. Assuming $\theta_L \ll 1$ and $\gamma \gg 1$, we can neglect the off-axis contribution of the incident photon direction and approximate $\theta'_L \rightarrow 0$. The resulting scattered photon has an energy $\epsilon'_f = (\omega'_f / \omega'_i) \epsilon'_i$ determined by Eq. A2, resulting in the scattered vector:

$$\vec{k}'_f = \frac{\epsilon'_f}{c} \begin{bmatrix} 1 \\ \sin \theta_s \cos \phi_s \\ \sin \theta_s \sin \phi_s \\ -\cos \theta_s \end{bmatrix} \quad (\text{A6})$$

Finally, transforming this back into the laboratory frame results in a final photon direction $\cos \theta$ and energy ϵ_f :

$$\cos \theta = \frac{\beta - \cos \theta_s}{1 - \beta \cos \theta_s} \quad (\text{A7})$$

$$\epsilon_f = \frac{\epsilon_i \gamma^2 (1 + \beta) (1 + \beta \cos \theta_L)}{1 + \gamma^2 \beta (1 + \beta) (1 - \cos \theta) + \frac{\epsilon_i}{m_e c^2} \gamma (1 + \beta \cos \theta_L) (1 + \cos \theta)} \quad (\text{A8})$$

The variation in photon energy with angle arises from the second term in the denominator. (For optical photons, the third term is negligible for $\gamma \lesssim 10^5$.) The median photon angle (produced at $\cos \theta_s \approx 0$) is $\theta = \cos^{-1} \beta$, or $\theta \approx 1/\gamma$ for $\gamma \gg 1$. In this limit the second term is to lowest order $\gamma^2 \theta^2$, as in Eq. 1, and the energy of the median scattered photon is half of the maximum energy. It can be shown from Equation A7 that in the high-energy limit, the scattering angle $\cos \theta_s \xrightarrow{\gamma \gg 1} (\theta^2 \gamma^2 - 1) / (\theta^2 \gamma^2 + 1)$, which is a function only of $(\theta \gamma)^2$. This explains why the scattered photon energy and probability density of scattering scale with this product, as shown in Figure 1.

The Klein-Nishina cross-section can be re-written in the laboratory frame as $d\sigma_{KN}/d\Omega = (d\sigma_{KN}/d\Omega')(d\Omega'/d\Omega)$, with the Jacobian term $(d\Omega'/d\Omega) = d \cos \theta_s / d \cos \theta = \gamma^{-2} (1 -$

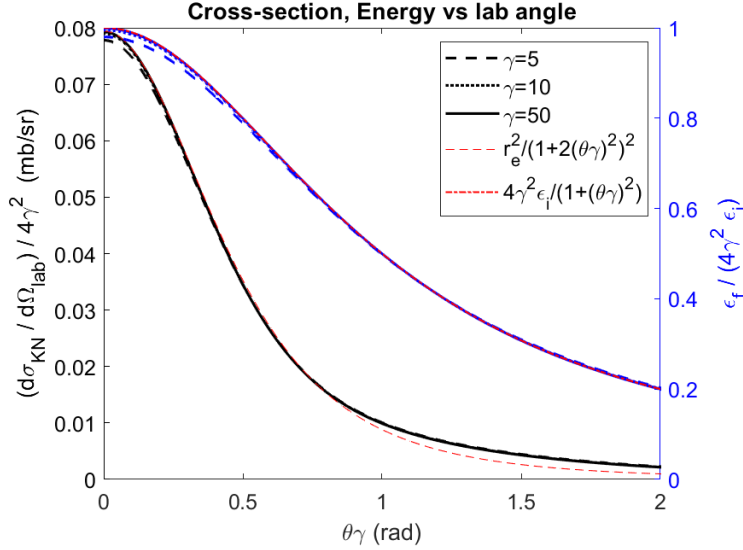


FIG. 5. Scattering cross-section normalized to $4\gamma^2$ (left, black) and scattered photon energy (blue, right) as functions of the scaled lab scattering angle $\theta\gamma$.

$\beta \cos \theta)^{-2}$. An analytical form is straightforward to calculate from Eq. A1 and A7, and is plotted as a function of $\theta\gamma$ in Figure 5. This is then integrated over laboratory solid angle to infer the photon fraction within a given acceptance angle (f) shown in Fig. 1b.

2. Electron-Laser Intersection Volume

To maximize the number of scattering events at a given intensity, the electron path inside the focused laser spot should be as long as possible. Assuming a Gaussian beam with radius at best focus $w_0 = 2f_{\#}\lambda/\pi$ and Rayleigh length $z_R = \pi w_0^2/\lambda$, the radius of the beam is $w(z) = w_0\sqrt{1 + (z/z_R)^2}$. The region with high intensity ($I > I_{max}/b$) is then a volume with the boundary:

$$\left(\frac{r}{w_0}\right)^2 = \left(1 + \frac{z^2}{z_R^2}\right) \left[\ln b - \frac{1}{2} \ln \left(1 + \frac{z^2}{z_R^2}\right)\right] \quad (\text{A9})$$

as shown in Figure 6a. The maximum path-length for an electron transiting this boundary depends on the angle of incidence ϕ (from Eq. 1). Taking $r = z \tan \phi$, we can solve for the path length $d = 2z/\cos \phi$ as shown in Figure 6b. The length of the interaction grows with reduced impact angle as $d \approx 2\sqrt{\ln b}/\phi$, up to a limiting value that depends on the Rayleigh length as $d_{max} = 2z_R\sqrt{b^2 - 1}$. (The scaling in Eq. 4 uses an intensity boundary of $b = \sqrt{2}$, such that $d_{max} = 2z_R$.) To take advantage of these long interaction volumes,

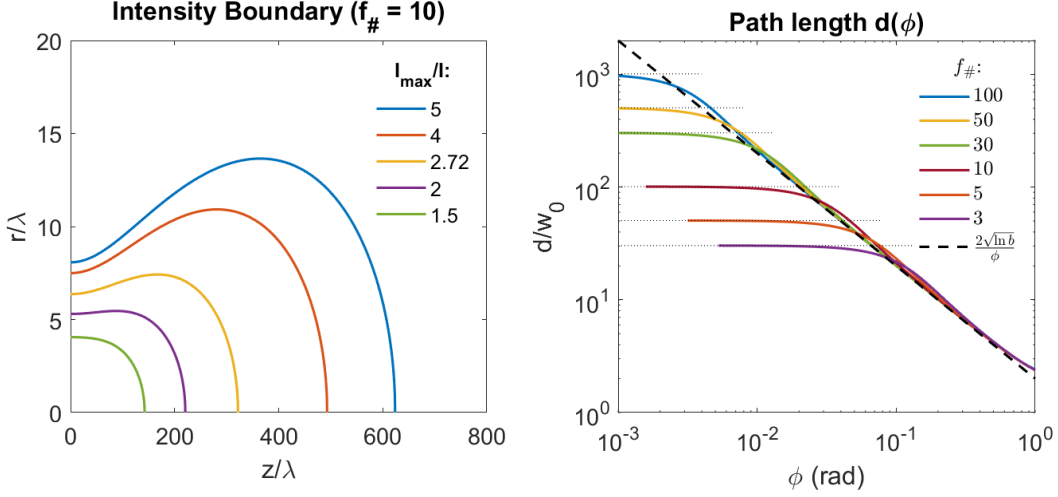


FIG. 6. (a) Intensity boundaries for a Gaussian laser pulse with $f_{\#} = 10$ ($w_0 = 6.37\lambda$). (b) Path length of an electron in the high-intensity region ($I_{\max}/I = e$) for different focal numbers $f_{\#} = \pi w_0/2\lambda$. Limiting path lengths for on-axis scattering are $2z_R\sqrt{e^2 - 1}$. To take advantage of long focal lengths ($f_{\#} > 20$), impact angle must be close to 0.

however, requires a collision angle close to $\phi = 0$. For example, at $\phi = 1^\circ$ (0.017 rad), there is no additional increase in the normalized path length with $f_{\#} \gtrsim 16$, which corresponds to $w_0/\lambda > 10$. This conclusion depends on the use of Gaussian beams: more realistic focusing schemes (for example, flat profiles in the far-field) must be evaluated.

If a flying focus pulse is used, the length of the intense region that co-moves with the electron packet is approximately twice the Rayleigh length, and the portion of the electron packet that can scatter at high intensity is limited to this length. For diffraction-limited focusing, $w_0 = 2f_{\#}\lambda/\pi$, the electron packet width is limited to $\tau \leq 4f_{\#}^2\lambda/\pi c = (f_{\#}^2)0.00447$ ps. For reasonable values of $f_{\#}$ this is much shorter than the values described in Sec. II A, and severely limiting the charge contained in the packets. In this case the photoinjector would be optimized for low emittance and the laser will be designed to achieve long interaction lengths and high intensities on axis.

Appendix B: Monte Carlo calculations

A Monte Carlo code was written in MATLAB to perform these calculations for an arbitrary distribution of initial electrons and photons. The four-vector transformations and

Klein-Nishina cross-section sampling are performed numerically for each photon-electron scattering event, with no scale approximations. This code will be used to simulate the effects of finite electron bandwidth, laser bandwidth, electron beam emittance, and laser focusing geometry. This approach does not account for the strong-field effects represented by a_0 terms in Eq. 1. However, for a given laser envelope, this effect may be approximated by accounting for the ponderomotive force on a scattering electron. This capability will be added and compared to more detailed electron radiation calculations described in the literature.

-
- [1] A. Alejo, G. M. Samarin, J. R. Warwick, and G. Sarri, Laser-wakefield electron beams as drivers of high-quality positron beams and inverse-compton-scattered photon beams, *Frontiers in Physics* **7**, 49 (2019).
 - [2] J. M. Kramer, A. Jochmann, M. Budde, M. Bussmann, J. P. Couperus, T. E. Cowan, A. Debus, A. Köhler, M. Kuntzsch, A. Laso García, U. Lehnert, P. Michel, R. Pausch, O. Zarini, U. Schramm, and A. Irman, Making spectral shape measurements in inverse Compton scattering a tool for advanced diagnostic applications, *Scientific Reports* **8**, 1398 (2018).
 - [3] S. Corde, K. Ta Phuoc, G. Lambert, R. Fitour, V. Malka, A. Rousse, A. Beck, and E. Lefebvre, Femtosecond x rays from laser-plasma accelerators, *Rev. Mod. Phys.* **85**, 1 (2013).
 - [4] D. H. Froula, D. Turnbull, A. S. Davies, T. J. Kessler, D. Haberberger, J. P. Palastro, S.-W. Bahk, I. A. Begishev, R. Boni, S. Bucht, J. Katz, and J. L. Shaw, Spatiotemporal control of laser intensity, *Nature Photonics* **12**, 262 (2018).
 - [5] Radiabeam Technologies, see <http://www.radiabeam.com>.
 - [6] M. J. Fitch, A. C. Melissinos, N. Barov, J.-P. Carneiro, H. T. Edwards, and W. H. Hartung, Compression of High-Charge Electron Bunches, arXiv:physics/0008206 (2000), arXiv:physics/0008206.
 - [7] Marmouget, J.-G, Binet, A., Guimbal, Ph., and Coacolo, J.-L., Present Performance of the Low-Emittance, High-Bunch Charge ELSA Photo-Injected Linac, *Proceedings of EPAC 2002*, 1795 (2002).
 - [8] K. Hirano, M. Fukuda, M. Takano, Y. Yamazaki, T. Muto, S. Araki, N. Terunuma, M. Kuriki, M. Akemoto, H. Hayano, and J. Urakawa, High-intensity multi-bunch beam generation by

- a photo-cathode rf gun, *Nuclear Instruments and Methods in Physics Research Section A: Accelerators, Spectrometers, Detectors and Associated Equipment* **560**, 233 (2006).
- [9] W. Theobald, C. Sorce, M. Bedzyk, S. T. Ivancic, F. J. Marshall, C. Stoeckl, R. C. Shah, M. Lawrie, S. P. Regan, T. C. Sangster, E. M. Campbell, T. J. Hilsabeck, K. Englehorn, J. D. Kilkenny, D. Morris, T. M. Chung, J. D. Hares, A. K. L. Dymoke-Bradshaw, P. Bell, J. Celeste, A. C. Carpenter, M. Dayton, D. K. Bradley, M. C. Jackson, L. Pickworth, S. R. Nagel, G. Rochau, J. Porter, M. Sanchez, L. Claus, G. Robertson, and Q. Looker, The single-line-of-sight, time-resolved x-ray imager diagnostic on OMEGA, *Review of Scientific Instruments* **89**, 10G117 (2018).
- [10] I. Drebot, A. Bacci, A. Bosotti, F. Broggi, F. Canella, P. Cardarelli, S. Cialdi, L. Faillace, G. Galzerano, M. Gambaccini, D. Giannotti, D. Giove, G. Mettievier, P. Michelato, L. Monaco, R. Paparella, G. Paternó, V. Petrillo, F. Prezl, M. Rossetti Conti, A. R. Rossi, P. Russo, A. Sarno, E. Suerra, A. Taibi, and L. Serafini, BriXs Ultra High Flux Inverse Compton Source Based on Modified Push-Pull Energy Recovery Linacs, *Instruments* **3**, 49 (2019).
- [11] R. Tikhoplav, *Low Emittance Electron Beam Studies*, Ph.D. thesis, University of Rochester (2006).
- [12] J. R. Rygg, J. H. Eggert, A. E. Lazicki, F. Coppari, J. A. Hawreliak, D. G. Hicks, R. F. Smith, C. M. Sorce, T. M. Uphaus, B. Yaakobi, and G. W. Collins, Powder diffraction from solids in the terapascal regime, *Review of Scientific Instruments* **83**, 113904 (2012), <https://doi.org/10.1063/1.4766464>.
- [13] M. Millot, F. Coppari, J. R. Rygg, A. Correa Barrios, S. Hamel, D. C. Swift, and J. H. Eggert, Nanosecond X-ray diffraction of shock-compressed superionic water ice, *Nature* **569**, 251 (2019).
- [14] F. Coppari, R. F. Smith, D. B. Thorn, J. R. Rygg, D. A. Liedahl, R. G. Kraus, A. Lazicki, M. Millot, and J. H. Eggert, Optimized x-ray sources for x-ray diffraction measurements at the omega laser facility, *Review of Scientific Instruments* **90**, 125113 (2019), <https://doi.org/10.1063/1.5111878>.
- [15] J. R. Rygg, R. F. Smith, A. E. Lazicki, D. G. Braun, D. E. Fratanduono, R. G. Kraus, J. M. McNaney, D. C. Swift, C. E. Wehrenberg, F. Coppari, M. F. Ahmed, M. A. Barrios, K. J. M. Blobaum, G. W. Collins, A. L. Cook, P. Di Nicola, E. G. Dzenitis, S. Gonzales, B. F. Heidl, M. Hohenberger, A. House, N. Izumi, D. H. Kalantar, S. F. Khan, T. R. Kohut, C. Kumar,

N. D. Masters, D. N. Polsin, S. P. Regan, C. A. Smith, R. M. Vignes, M. A. Wall, J. Ward, J. S. Wark, T. L. Zobrist, A. Arsenlis, and J. H. Eggert, X-ray diffraction at the national ignition facility, *Review of Scientific Instruments* **91**, 043902 (2020), <https://doi.org/10.1063/1.5129698>.